



Impact of Temperature and Discharge Rate on the Aging of a LiCoO₂/LiNi_{0.8}Co_{0.15}Al_{0.05}O₂ Lithium-Ion Pouch Cell

Yao Wu,^{*,z} Peter Keil,^{*} Simon F. Schuster, and Andreas Jossen

Institute for Electrical Energy Storage Technology, Technical University of Munich, 80333 Munich, Germany

This paper presents a lithium-ion battery aging study in which pouch cells comprising a LiCoO₂/LiNi_{0.8}Co_{0.15}Al_{0.05}O₂ blended cathode and a graphite anode are examined. The study focuses on the impact of temperature and discharge rate on the cycle life of the tested cells. Compared to the aging behavior of other lithium-ion cells in the literature, the cells tested here are less sensitive to the discharge rate but more vulnerable to low temperature cycling. The vulnerability to low temperature mainly comes from cathode degradation, especially of the LiCoO₂ component. This is identified by electrochemical impedance spectroscopy, differential voltage analysis and incremental capacity analysis. The cells are able to achieve 3000–5000 cycles before reaching a capacity fade of 20%, also at higher discharge rates up to 5C. All in all, the high discharge rate capability could be a general advantage of pouch cells due to less mechanical and thermal stress in their geometry. Furthermore, more attention should be paid to the cathode health in low temperature applications of lithium-ion cells containing layered oxides. This paper focuses mainly on non-invasive aging detection methods for lithium-ion cells. Post-mortem results will be published in a following paper.

© The Author(s) 2017. Published by ECS. This is an open access article distributed under the terms of the Creative Commons Attribution 4.0 License (CC BY, <http://creativecommons.org/licenses/by/4.0/>), which permits unrestricted reuse of the work in any medium, provided the original work is properly cited. [DOI: 10.1149/2.0401707jes] All rights reserved.



Manuscript submitted December 14, 2016; revised manuscript received March 20, 2017. Published May 5, 2017.

Lithium-ion batteries play an important role in the development of electrification in modern society. They are already employed in a wide range of application areas from electric vehicles to consumer electronics. Compared to consumer electronics, electric vehicles have more stringent demands on the lifetime performance of lithium-ion batteries. In order to improve the reliable application of lithium-ion batteries in the automotive field, a profound understanding of their aging behavior is essential. In the past decades, there have been studies with efforts to explain the aging behavior of lithium-ion batteries.^{1–5} Wang et al. established a cycle life model including temperature, depth of discharge (DOD) and discharge rate based on a graphite-LiFePO₄ cell.¹ Ecker et al. developed a semi-empirical calendar aging model depending on temperature and state of charge (SoC) of a graphite-LiNi_{1/3}Mn_{1/3}Co_{1/3}O₂ cell.³ Nonetheless, due to a variety of electrode materials, cell geometries and electrolyte compositions, one is still far away from a fundamental understanding of the aging behavior of lithium-ion cells.

The aging of lithium-ion cells depends not only on the time or cycle number, but also on the operational conditions, i.e. stress factors. An in-depth analysis of the influence of decisive stress factors, including temperature, charge/discharge rate, DOD and average SoC, is a prerequisite to prolong the life span and ensure the performance reliability of lithium-ion cells.

Temperature has a strong impact on the cycle aging rate of lithium-ion batteries. The best cycle life can be obtained for moderate temperatures, because low temperatures decrease cycle life due to intensified lithium plating and high temperatures reduce battery life due to Arrhenius-driven aging reactions.⁶ Waldmann et al.⁷ conducted a comprehensive experiment covering a temperature range from –20°C to 70°C and discovered 25°C as the optimal temperature regarding the cyclic aging behavior of 18650-type cells with a Li_xNi_{1/3}Mn_{1/3}Co_{1/3}O₂/Li_yMn₂O₄ blended cathode and graphite/carbon anode. As shown by other research work, the optimal cycling temperature can differ from 25°C. It varies with the cell type. Schuster et al.⁵ reported the optimum to be at 35°C, whereas Bauer et al.⁸ detected it to be around 17°C. Temperatures higher than the optimum contribute to an accelerated solid electrolyte interphase (SEI) formation, thus a more rapid capacity fade and impedance rise. Lower temperatures favor lithium plating at the end of the charging process. Many researchers^{9–13} have identified lithium plating using either in-situ or ex-situ methods in cycled lithium-ion cells at low temperature, but none of them has reported cathode degradation under this condition.

The discharge rate was often reported to have an exponential influence on the aging rate of lithium-ion cells.^{1,14–17} Cui et al.¹⁷ determined the relationship between discharge rate and capacity loss on the prismatic 1.15 Ah LiCoO₂/MCMB (mesocarbon microbeads) lithium-ion cells in Eqs. 1–3.

$$Q_{loss}(T, C, n) = A(C) \exp\left(-\frac{E_a(C)}{8.314T}\right) n^{0.740} \quad [1]$$

$$A(C) = \exp(4.33C^2 - 3.37C + 5.03) \quad [2]$$

$$E_a(C) = 2.330 \times 10^3 \exp(1.337C) + 1.353 \times 10^4 \quad [3]$$

Here, Q_{loss} is the capacity loss, T is the absolute temperature in Kelvin, C is the discharge rate, n is the cycle number, $A(C)$ is the pre-exponential factor, and $E_a(C)$ is the activation energy.

Omar et al.¹⁶ also reported an exponential influence of discharge rate on the cycle life of the cylindrical 2.3 Ah LiFePO₄/graphite lithium-ion cells. Wang et al.¹ extracted a similar battery life time model as the aforementioned Cui group with discharge rate in the exponent in Eq. 4. The result was based on a large cycle test matrix of 2.2 Ah, 26650 cylindrical LiFePO₄/graphite lithium-ion cells.

$$Q_{loss} = B \cdot \exp\left(\frac{-31700 + 370.3 \times C_{Rate}}{RT}\right) Ah^{0.55} \quad [4]$$

Where Q_{loss} is the capacity loss, B is the pre-exponential factor, C_{Rate} is the discharge rate, R is the gas constant, T is the absolute temperature in Kelvin, and Ah is the Ah-throughput. Eqs. 1 and 4 are empirical models, hence the units on both sides of the equal signs are not strictly identical.

Many researchers hold the view that high current discharge induces cracks in SEI layer, which is followed by SEI repair.^{1,14,16,18,19} Therefore, the side reactions on the anode surface are accelerated and the passive layer grows further. All these processes increase the consumption of cyclable lithium and the impedance of the cell. In reality, higher cell temperatures always come along with higher discharge rates, which blurs the true reason for the accelerated cell aging under high discharge current. This paper investigates the influence of the stress factors temperature and discharge rate on a lithium-ion pouch cell with a blended cathode.

Blended cathodes are developed to combine the advantages of different cathode materials. Some research groups have made attempts to explain the aging mechanisms of the blended cathode LiMn₂O₄/LiNi_{1/3}Mn_{1/3}Co_{1/3}O₂.^{2,20,21} They have revealed that the aging mechanisms in those cells are mainly loss of cyclable lithium

*Electrochemical Society Student Member.

^zE-mail: yao.wu@tum.de

and partially loss of cathode material. However, there is little information about the aging behavior of $\text{LiCoO}_2/\text{LiNi}_{0.8}\text{Co}_{0.15}\text{Al}_{0.05}\text{O}_2$ (LCO/NCA) blended cathodes.

Experimental

To investigate the impact of the stress factors of temperature and discharge rate on lithium-ion batteries, lithium-ion pouch cells of the type SLPB50106100 with a nominal capacity of 5 Ah from the manufacturer Kokam were examined. According to energy-dispersive X-ray spectroscopy results, the active materials of the cell are composed of graphite at the anode and blended material LCO/NCA at the cathode. In the data sheet, a voltage range from 2.7 V to 4.2 V and maximum current rates of 2C and 5C for charging and discharging are recommended, respectively.

In our aging experiment, performance tests were carried out periodically to check the state of health (SoH) of the cells. The performance tests were divided into basic performance tests and extended performance tests. The basic performance test, i.e. a capacity test, was carried out every two weeks. The extended performance test was conducted every four weeks, including a capacity test, an open circuit voltage (OCV) test and an electrochemical impedance spectroscopy (EIS) test. Cycling tests, capacity tests and OCV tests were conducted with a Cell Test System (CTS) by BaSyTec. EIS tests were done on a potentiostat VMP3 by Biologic Science Instruments. All these tests were performed in climate chambers at 25°C. The cells were tested under regular atmospheric pressure. No additional external pressure was applied.

In the capacity test, the remaining capacity was measured as follows. Cells were charged with a constant current (CC) of 1C (corresponding to 5 A) to 4.2 V and then switched to a constant voltage (CV) at 4.2 V. When the current dropped below 0.05C in the CV phase, cells were considered as 100% charged. After a pause of 10 min, a CC of 1C was applied to discharge the cells to 2.7 V, followed by a CV phase to further discharge the cell until the current fell below 0.05C. The purpose of this CV phase was to minimize the influence of impedance rise in the cells on the measured capacity. The OCV tests were always started 10 h after the preceding capacity test to exclude an influence of relaxation on the OCV curves. A CC of 0.1C was implemented to charge the cells to 4.2 V and then the same CV charge phase as above was employed. After a pause of 1 h, the cells were discharged with a 0.1C CC to 2.7 V and with the same CV discharge phase as above. The impedance spectrum was measured 6 h after the OCV test in galvanostatic mode from 100 kHz to 10 mHz with an AC amplitude of 200 mA at 50% SoC. The real part of the impedance at the zero crossing in the Nyquist plot was taken as the ohmic resistance of the cell.

Table I provides an overview of the aging test matrix. For the temperature test series, 10°C, 25°C and 40°C were chosen. In the cycling profile, cells were charged with a 1C CC-CV procedure and discharged with a 1C CC procedure at each temperature. The charging process was switched from CC to CV at 4.2 V and the CV process was stopped when the current dropped below 0.05C. The discharging process was stopped at 2.7 V. For the discharge rate test series, all cells were tested at 25°C. The discharge procedure was changed to 3C and 5C CC discharge respectively, whereas the charge procedure was kept the same. At least two cells were tested under each aging condition and their averaged performance is presented together with the span of maximum and minimum values in the following sections.

Table I. Aging test matrix for investigating the stress factors temperature and discharge rate.

	10°C	25°C	40°C
1C Discharge	x	x	x
3C Discharge		x	
5C Discharge		x	

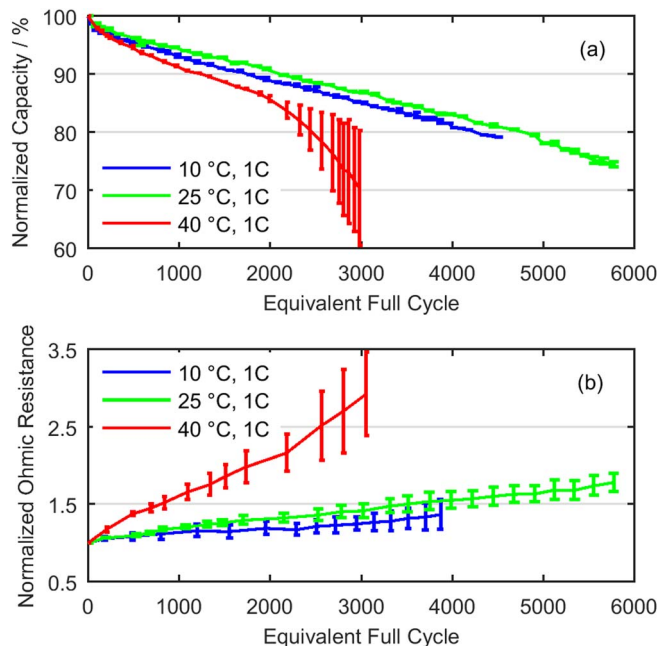


Figure 1. Results from the performance tests at 25°C: (a) Normalized capacity plotted as a function of equivalent full cycle, (b) normalized ohmic resistance plotted as a function of equivalent full cycle. Data are shown for the cells cycled with 1C at 10°C, 25°C and 40°C.

Results and Discussion

In order to investigate the aging behavior of the LCO/NCA-graphite-based cells, the evolution of cell performance parameters, i.e. discharge capacity and ohmic resistance, are extracted and compared under all operational conditions. Moreover, EIS, differential voltage analysis (DVA) and incremental capacity analysis (ICA) are employed as aging detection methods to reveal the relevant aging mechanisms.

Effect of the temperature.—The aging behavior of cells tested at different temperatures is presented in this section. Fig. 1a shows the normalized discharge capacity versus equivalent full cycle (EFC) at the three ambient temperatures. Table II presents the minimum, maximum, and average cell surface temperature for the different cycling conditions. The three ambient temperatures, i.e. 10°C, 25°C and 40°C, correspond to the average cell surface temperatures of 10.1°C, 27.5°C and 41.5°C during cycling, respectively. These temperature data were taken from the last cycling tests before the cells reached 20% capacity loss. These values can be considered as worst-case values, as the cells had lower internal resistances in the earlier cycling tests. At the beginning, all tested cells have an average discharge capacity (CC+CV) of 5.709 Ah, with a deviation of $\pm 0.26\%$. In the first 300 cycles, there is a root-function-like capacity fade for all tested cells. Afterwards, the capacity decreases linearly in all cases yet at different rates. Cycling at 25°C is the mildest operational condition with the lowest capacity

Table II. Surface temperature of cells during their last cycling tests before 20% capacity loss.

	Minimum Temperature	Average Temperature	Maximum Temperature
1C Discharge, 10°C	8.4°C	10.1°C	15.4°C
1C Discharge, 25°C	25.3°C	27.5°C	33.1°C
1C Discharge, 40°C	39.6°C	41.5°C	44.2°C
3C Discharge, 25°C	26.4°C	30.2°C	40.2°C
5C Discharge, 25°C	26.4°C	31.1°C	49.3°C

degradation rate over EFC. Cycling at 10°C and 40°C both accelerate the capacity fade. The capacity deviation of the different cells tested under identical load conditions is generally negligible, proving the excellent cell quality. An exception are those cells cycled at 40°C after more than 15% capacity loss. Here, a split of two aging curves is observed. One cell continues to lose its capacity linearly over EFC. The other cell shows a roll-over effect in cell capacity fade.

Fig. 1b shows the normalized ohmic resistance versus EFC. The data were taken from the EIS measurements. At the beginning, the average ohmic resistance was 2.7 mΩ, with a deviation of $\pm 5\%$. The ohmic resistance increases linearly from the very beginning in all cases. In contrast to the capacity fade in Fig. 1a, the increase of the ohmic resistance aggravates with increasing temperature, indicating different aging mechanisms responsible for the capacity fade and ohmic resistance increase. The resistance deviation is larger than the capacity deviation and expands gradually over EFC. In the case of the cells cycled at 40°C, the resistance evolution also divides into two degradation modes, with one continuous linear increase and the other accelerated increase. This coincides with their capacity evolution.

A linear dependency of the cell capacity on the EFC has been reported in many studies.^{4,20,22} The aging mechanisms in this linear area could be categorized into cycle induced capacity loss and calendar aging based capacity loss. The cycle induced capacity loss refers to the lithium consumption caused by the cycle-triggered cracks on the anode particles and the additional SEI formation. The calendar aging based capacity loss is related to temperature-accelerated chemical parasitic reactions which consume lithium, e.g. formation and reconstruction of SEI.²⁰ A higher capacity fade rate at 10°C than at 25°C is possibly a result of lithium plating,^{7,8} since internal electrode resistances increase with lower temperature and the anode potential eventually drops to potentials negative to reversible Li/Li⁺ potential.²³

The ohmic resistance originates from the bulk chemistry of a cell, including resistance of the electrolyte, active materials and current collectors.^{5,24–27} The ohmic resistance increase mainly originates from the decomposition of electrolyte, including both conductive salt and solvent, which in turn changes the electrolyte conductivity.^{21,28–30} The cell cycled at 40°C with a higher aging rate and a new cell were disassembled. This revealed that the aged cell had dried out, as no traces of electrolyte wetting the electrodes and the separator were visible any longer. The absence of visible liquid electrolyte leads to the assumption that electrolyte decomposition is the reason for the marked capacity fade and resistance increase. Furthermore, plated lithium was also observed on the aged anode layers, which is usually not expected at a temperature of 40°C. This hints a relationship between the roll-over effect of cell capacity fade and lithium plating as has already been investigated in Ref. 5.

Effect of the discharge rate.—The effect of discharge rates on the aging behavior of the tested cells is described here. Fig. 2a shows the normalized discharge capacity versus EFC at 25°C ambient temperature with the three discharge rates 1C, 3C and 5C. As shown in Table II, average cell surface temperatures of 27.5°C, 30.2°C and 31.1°C were calculated for 1C, 3C and 5C discharge cycling, respectively. Similar to Fig. 1a, the capacity fades notably in the first 300 cycles and afterwards, the capacity decreases quasi linearly in all cases. All the capacity fade curves run almost parallel after 300 cycles till end-of-life. The influence of the elevated average cell surface temperature and the influence of the higher discharge rate on the aging rate cannot be separated from each other. 1C cycling has a cycling life of about 4800 EFC, while 5C cycling achieves around 3500 EFC. The capacity deviation remains imperceptible, except for the cells cycled at 5C near the end-of-life.

Fig. 2b shows the evolution of ohmic resistance versus EFC at 25°C ambient temperature for the three cycling discharge rates. The ohmic resistances of 3C and 5C, unlike that of 1C, increase rapidly at the beginning, moderately afterwards and again strikingly near the end-of-life. It's noteworthy that the cells cycled with 5C discharge rate double their ohmic resistances very quickly. The resistance deviation of 3C and 5C cycling is much larger than that of 1C cycling and

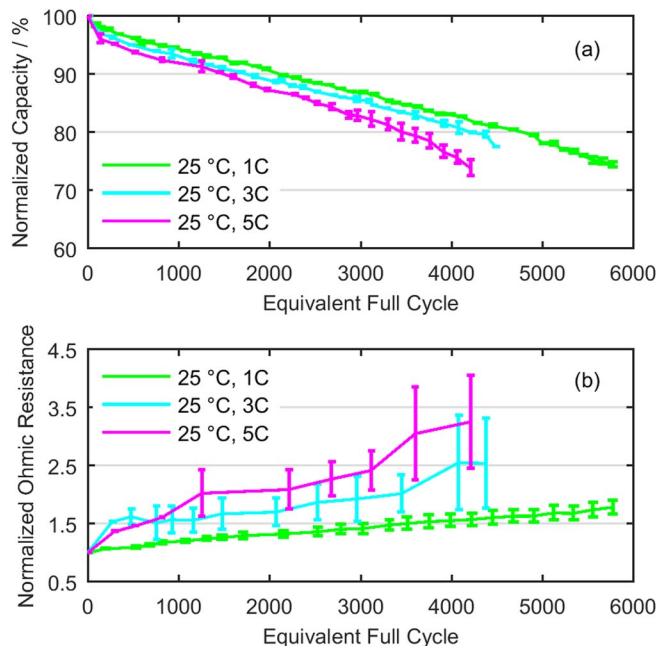


Figure 2. Results from the performance tests at 25°C: (a) Normalized capacity plotted as a function of equivalent full cycle, (b) normalized ohmic resistance plotted as a function of equivalent full cycle. Data are shown for the cells cycled with 1C, 3C and 5C at 25°C.

grows with aging. Lithium-ion pouch cells have generally low ohmic resistance compared to 18650-type lithium-ion cells. The cells cycled at 5C show a maximum ohmic resistance of 11.3 mΩ at the end-of-life, which corresponds to more than three times the initial ohmic resistance.

A similar linear capacity fade rate is observed for the different discharge rates, implying similar aging mechanisms for all three cases. It is supposed that high discharge rates cause rapid volume changes, which break the SEI layer and induce more electrolyte decomposition, thus more capacity is lost in the first 300 cycles at 3C and 5C. Afterwards, the capacity aging rates of 1C, 3C and 5C are approximately identical, which hints a stabilization of the SEI layer and a constant SEI growth rate.^{14,18,19} The higher cell temperatures at 3C and 5C may have also helped the stabilization of the SEI in the first few hundred cycles.

Electrochemical impedance spectroscopy.—In order to get a profound understanding of the aging mechanisms of the tested cells, Nyquist plots acquired from the EIS measurements are presented in Fig. 3. Since the ohmic resistance is the real part of the impedance at zero crossing in a Nyquist plot and its evolution has already been shown in the two previous subsections, the Nyquist plots in Fig. 3 are all normalized to the beginning zero crossing point in each case to give a better comparison of their resistances from medium to low frequencies.

In these Nyquist plots, two superimposed semi-circles and a sloping line can be observed. According to the literature, the semi-circle at higher frequencies originates largely from the anode and is ascribed to the SEI layer.^{24–27,31–34} the semi-circle at medium frequencies represents mainly the double layer capacity and the charge transfer resistance of the cathode^{33,35–38} and the slope at lower frequencies can be attributed to diffusion-limited processes.^{34,37,39,40}

Figs. 3a, 3b and 3c show the Nyquist plots of cells cycled at 10°C, 25°C and 40°C. Four representative aging states are depicted. These are: begin of test (BOT), 850 cycles, 3300 cycles and 5000 cycles. The semi-circle at higher frequencies stays unchanged at 10°C and 25°C and increases gradually at 40°C. This confirms an intensified SEI growth at higher temperature, which has also been reported by other research groups.^{8,41–44} The temperature dependency of the SEI

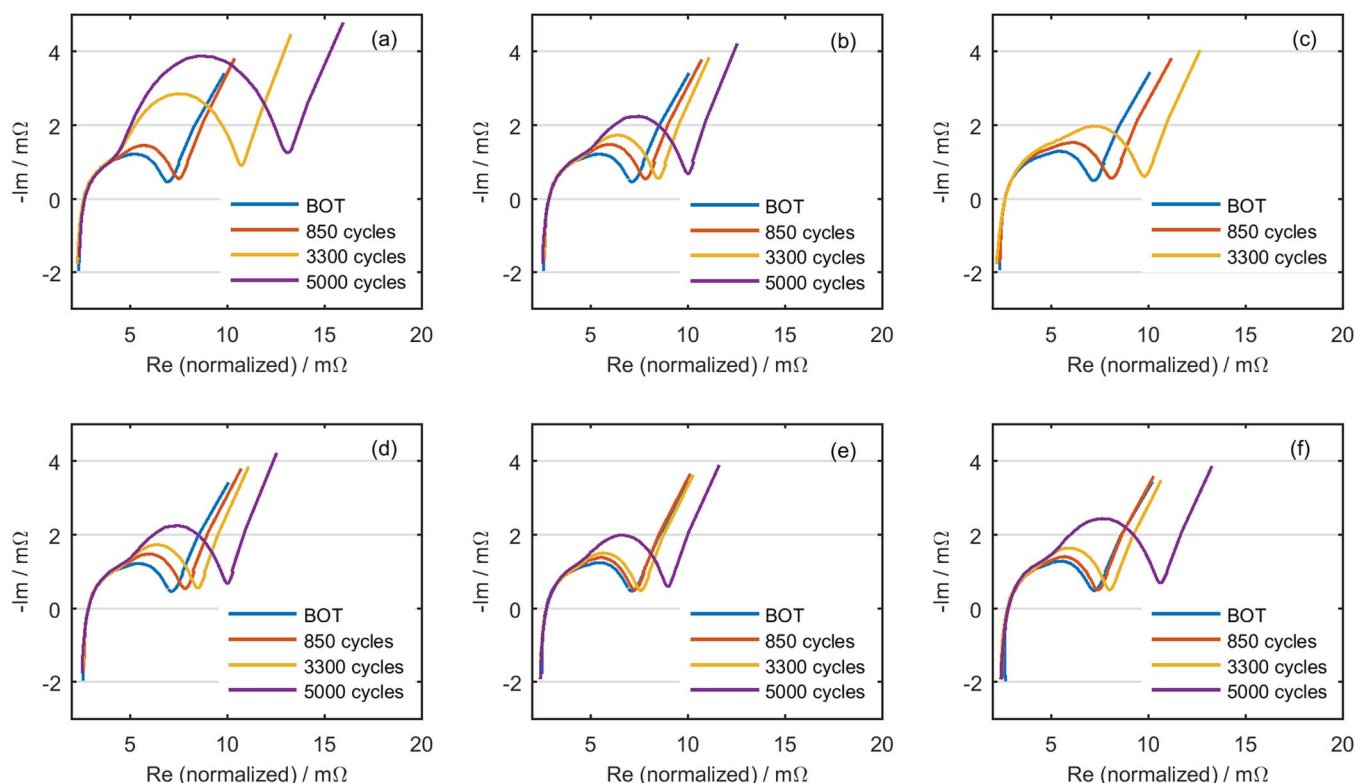


Figure 3. Normalized Nyquist plots of a cell cycled at (a) 10°C, 1C; (b) 25°C, 1C; (c) 40°C, 1C; (d) 25°C, 1C; (e) 25°C, 3C; (f) 25°C, 5C. All spectra of cycled cells have been left-shifted to the same zero-crossing of the x-axis as the spectrum at the begin of test (BOT).

growth is comprehensible, since the SEI growth comprises chemical reactions, like electrolyte decomposition and organic/inorganic compounds formation, which can be accelerated by high temperature.^{45,46}

The semi-circle at medium frequencies increases enormously after 850 cycles at 10°C. In the cases of 25°C and 40°C, the semi-circles at medium frequencies both increase steadily and 40°C show a faster increase. The cycling of the cell (the one with less capacity fade of the two tested cells in Fig. 1) at 40°C was stopped at about 3500 cycles due to a damage to the cell connection. Therefore, Fig. 3c shows only the aging states until 3300 cycles. The charge transfer resistance originates from the interface of electrolyte and electrodes, particularly the cathode side.^{47–52} Passive layer growth and phase transitions on the cathode surface lead to a continuous increase of the charge transfer resistance. The massive charge transfer resistance increase at 10°C may be a crucial cathode structural disordering, which will be verified in the following section by means of DVA and ICA.

Figs. 3d, 3e and 3f show the influence of discharge rates on the impedance spectra. Figs. 3b and 3d are identical. 1C discharge at 25°C is displayed twice to keep the appropriate comparison sequence. The semi-circle at higher frequencies keeps almost unchanged for all three discharge rates. The growth of the semi-circles at medium frequencies is suppressed by higher discharge rates at first. Only after 3300 cycles, i.e. shortly before the end-of-life, they experience an abrupt increase. The suppression effect could be possibly explained by earlier cutoff of the CC discharge process at 3C and 5C, thus the cathode is less stressed by a high degree of lithiation. After 3300 cycles, severe cathode degradation takes place and hinders the charge transfer process.

Differential voltage analysis.—The Clauss group⁵³ firstly introduced the method ICA in 1976 to plot the differential capacity dQ/dU versus the cell potential U , thus indistinct voltage plateaus can be transferred into distinguishable peaks. Dubarry et al. have performed a series of aging characterization work by means of ICA on a wide range of cell chemistries.^{2,41,54–61} The DVA is the inverse of ICA,

with dU/dQ versus capacity Q . It has been employed by Bloom et al.^{62–65} and Dahn et al.⁶⁶ for non-invasive aging analysis. The DVA of a full cell has been proven to be the superposition of the DVAs of both electrodes.⁶⁵ ICA and DVA both require CC charge or discharge data with a small current rate, typically C/25, to ensure a close-to-equilibrium state of the cell.⁶⁷ Some researchers also apply a current rate of C/3 to reduce the test time.^{68,69}

In a lithium-ion cell, the anode and the cathode can be considered as serial connected voltage sources, therefore the battery OCV is the difference of both electrode potentials. This is the theoretical basis of the DVA superposition principle, as shown in Eqs. 5 and 6.

$$U_{cell}(Q) = U_{cathode}(Q) - U_{anode}(Q) \quad [5]$$

$$\frac{dU_{cell}}{dQ} = \frac{dU_{cathode}}{dQ} - \frac{dU_{anode}}{dQ} \quad [6]$$

In the case of a blended cathode, its components are parallel connected voltage sources, thus the cathode capacity is the addition of both component capacities. After differentiation, we get the superposition principle of ICA curves for both cathode components in Eqs. 7 and 8.^{70,71}

$$Q_{blend}(U) = \alpha \cdot Q_{LCO}(U) + \beta \cdot Q_{NCA}(U) \quad [7]$$

$$\frac{dQ_{blend}}{dU} = \alpha \cdot \frac{dQ_{LCO}}{dU} + \beta \cdot \frac{dQ_{NCA}}{dU} \quad [8]$$

Firstly, in order to separate the influences from both electrodes, a new Kokam cell was disassembled and half cells were built out of its electrodes versus metal lithium. The anode half cell was cycled between 0.01 V and 1.5 V with a current of C/50. The cathode half cell was cycled between 2.7 V and 4.3 V with a current of C/50. Figs. 4a and 4b present those half cell voltage curves and DVA curves that correspond to the charging of the full cell. The full cell DVA curve in

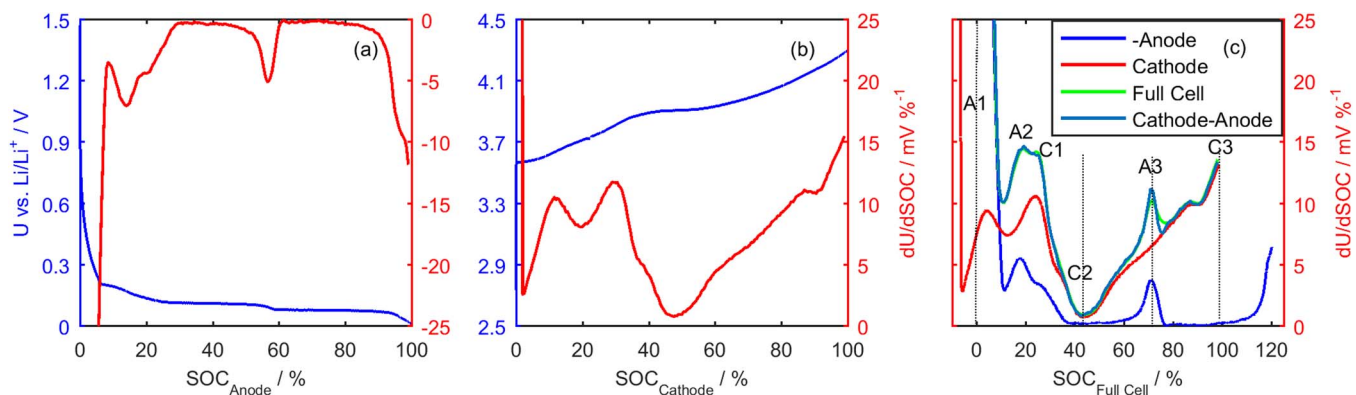


Figure 4. Half cell voltage curves and the resulting DVA curves of (a) anode and (b) cathode, which correspond to the charging of the full cell. (c) Superposition of both half cell DVA curves and comparison with the full cell DVA curve.

Fig. 4c was calculated from the charge voltage curve of the full cell with a current of $C/10$ from 2.7 V to 4.2 V. As illustrated in Fig. 4c, the peaks in the charge DVA curve of a full cell can be attributed to both electrodes according to the DVA superposition principle in Eq. 6. These distinguishable peaks, valleys or ends are marked conforming to their electrode origins as A1, A2, A3, C1, C2 and C3. The x-axis distances between peaks, valleys or ends from the same electrode can be used to determine changes in the amount of active material of this electrode.

Fig. 5 shows the evolution of charge DVA curves of cells tested under all operational conditions. These DVA curves were calculated from the charge voltage curves of their corresponding full cells with a current of $C/10$ from 2.7 V to 4.2 V. Figs. 5a, 5b and 5c show the charge DVA curves of cells cycled with 1C at 10°C, 25°C and 40°C, while Figs. 5d, 5e and 5f show those cells cycled at 25°C with 1C, 3C and 5C discharge rates. The chosen cycle numbers are identical with those from Fig. 3. Except for Fig. 5a, all cases show an almost

parallel shift of the cathode contributions to the left. This indicates a loss of cyclable lithium according to the literature.^{72,73} In Fig. 5a, the slope between around 40% to 100% SoC, which is characteristic for the cathode according to Fig. 4c, flattens with cycles, indicating changes in the cathode structure.

Since the cathode consists of LCO and NCA, $C/20$ constant current charge voltage data of these cathode materials were taken from literature⁶⁶ for further analysis. The ICA curves of LCO and NCA and their superposition result are shown in Fig. 6a. The ICA curve of blended cathode in Fig. 6a was calculated from the cathode half cell charge voltage curve from Fig. 4b. The fitting result suggests a capacity ratio of 0.44:0.56 (LCO:NCA). According to Fig. 6a, the ICA peak at around 3.9 V can be attributed to LCO. The voltage curve around 3.9 V correspondingly receives dominant influence from LCO. Fig. 6b shows the DVA curves of the blended cathode and the LCO+NCA fitting. The curve from fitted literature data is in good agreement with the half cell measurement of the actual blended cathode material. The

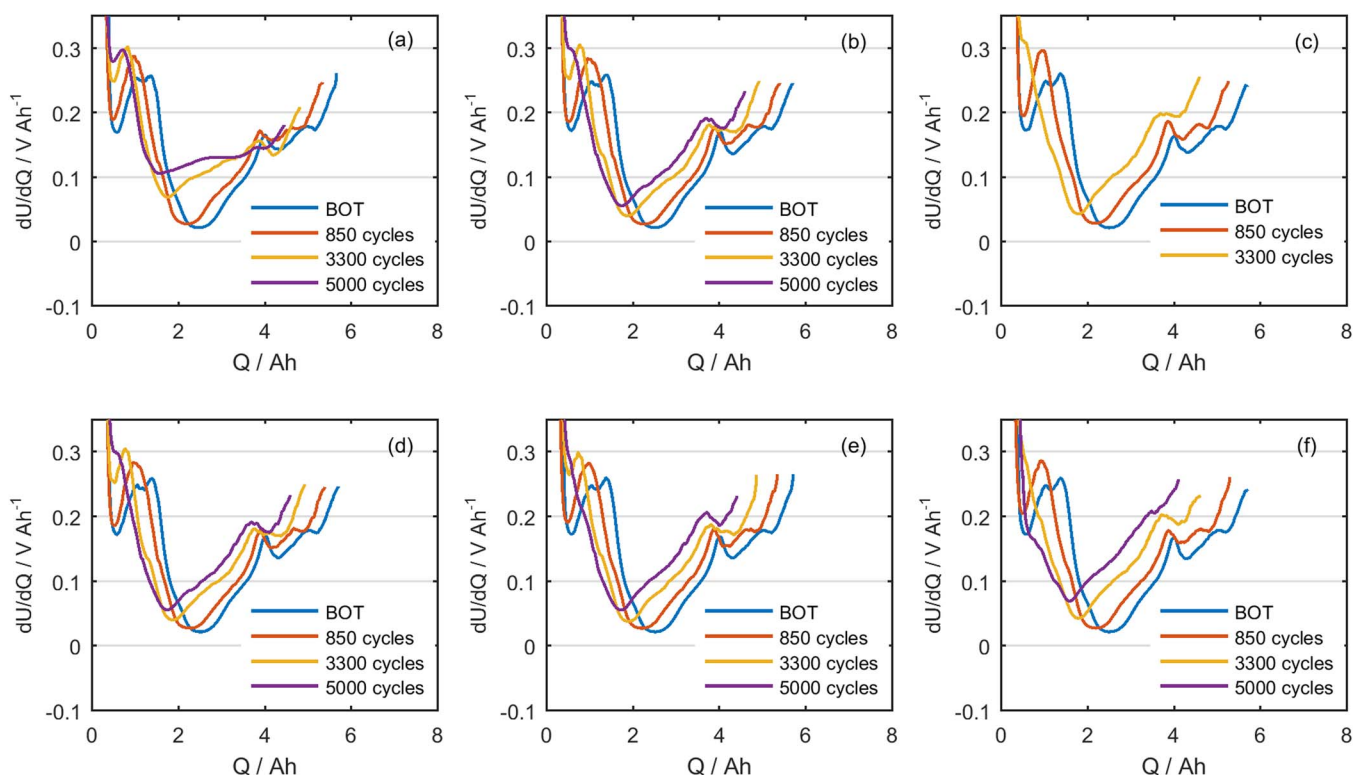


Figure 5. DVA curve evolution of a cell cycled at (a) 10°C, 1C; (b) 25°C, 1C; (c) 40°C, 1C; (d) 25°C, 1C; (e) 25°C, 3C; (f) 25°C, 5C.

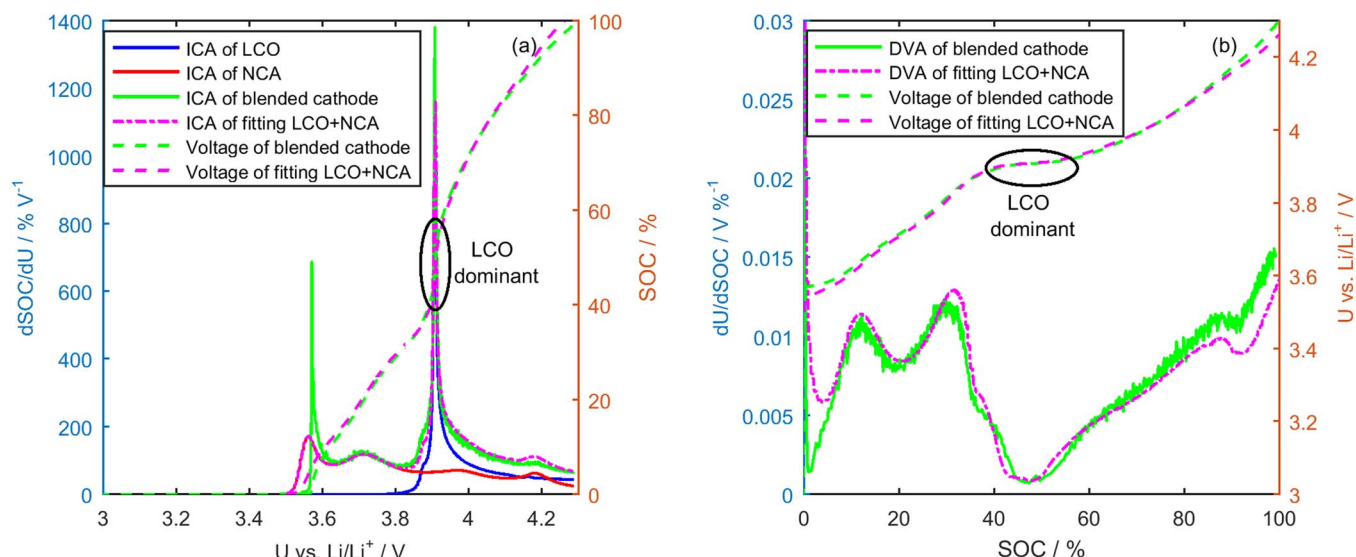


Figure 6. (a) ICA curves of both cathode components and their superposition fitting result compared with the actual blended cathode measurements; (b) the fitting result from (a) is transferred into DVA curves.

flat voltage plateau, which leads to the valley in the DVA spectra depicted in Fig. 5, corresponds to the dominant LCO peak in the ICA spectra. Fig. 7 shows a comparison of the charge ICA curve evolution of one cell cycled at 10°C and one cell cycled at 25°C. The offsets in the region of 3.4–3.6 V are similar between both subplots, but the peak at 3.8 V shrinks much faster in Fig. 7a than in Fig. 7b. According to Ref. 74, the combination of the offset in region 3.4–3.6 V and the peak shrinkage at 3.8 V could be a result of loss of lithium inventory (LLI). However, LLI alone could not explain the difference between Fig. 7a and Fig. 7b, otherwise both cells should share similar behavior in the whole region of 3.4–3.9 V. There must be additional degradation, which leads to more peak shrinkage at 3.8 V in Fig. 7a. This 3.8 V-peak originates from the LCO-dominant potential plateau between SOC_{Cathode} 40%–55% in Fig. 4b facing the graphite potential plateau

between SOC_{Anode} 25%–55% in Fig. 4a. The graphite anode experiences little loss in both cases, since the area under the ICA curves between 3.0 V and the graphite stage-2 → stage-1 arch keeps almost the same. Hence, it is reasonable to conclude that LCO degradation exists along with LLI in the cell of Fig. 7a. This LCO degradation is probably related to the vast increase in the charge transfer semi-circle in Fig. 3a.

As described in Fig. 4c, A1, A2, A3, C1, C2 and C3 are attributes of the anode and the cathode, respectively. Q_{Anode} , defined as the x-axis distance between A1 and A3, reveals changes in the anode active material capacity. Q_{Cathode} , defined as the x-axis distance between C2 and C3, reveals changes in the cathode active material capacity. Q_{Cell} , defined as the x-axis distance between A1 and C3, is the full cell capacity. Unfortunately, the positions of C1 and C2 will be difficult to detect due to the interaction of the anode and cathode DVA curves when LLI takes place (offset between both DVA curves). Therefore, Q_{Cathode} change cannot be determined during the cycling test using this method.

The DVA curves from Fig. 5 are firstly smoothed to remove noise using the Moving Average Filtering. Then, the exact positions of A1, A3 and C3 are detected by the Findpeaks function in MATLAB. At last, the Q_{Anode} and Q_{Cell} values are plotted in Fig. 8. It is not intended to measure the precise and absolute capacity amount of anode with Q_{Anode} , but to identify the tendency of anode active material change.

As illustrated in Fig. 8, the anode loss is within 10%, except for 5C discharge cycling. In Fig. 4c, the anode has an excess of 20% capacity compared to the full cell at the beginning. Hence, the anode loss is not an origin of full cell capacity decrease. In Fig. 8, Q_{Cell} decreases almost linearly in all cases between 80% and 95% capacity retention. Due to the lack of Q_{Cathode} , it is not possible to separate the cathode loss from LLI.

Conclusions

This aging study has investigated the influence of temperature and discharge rate on the aging characteristic of a lithium-ion pouch cell with a blended cathode LCO/NCA. As for the temperature test, results show that high temperature (>25°C) accelerates the aging caused by hastened SEI layer growth. A drying-out of the cell due to electrolyte decomposition was observed. Low temperature (<25°C) increases the aging due to enormous charge transfer resistance increase from the degraded LCO cathode component. At 10°C, no signs of lithium plating were observed. As for the discharge rate test, this pouch cell

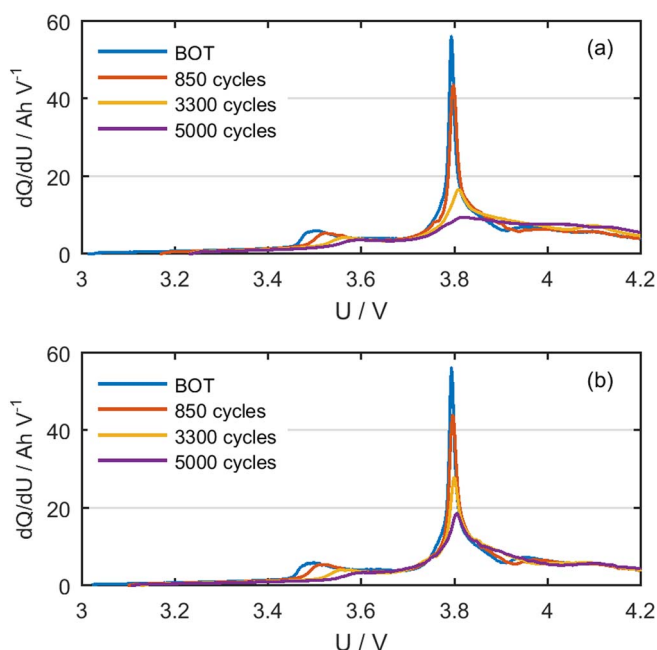


Figure 7. ICA curve evolution of a cell cycled at (a) 10°C, 1C and (b) 25°C, 1C.

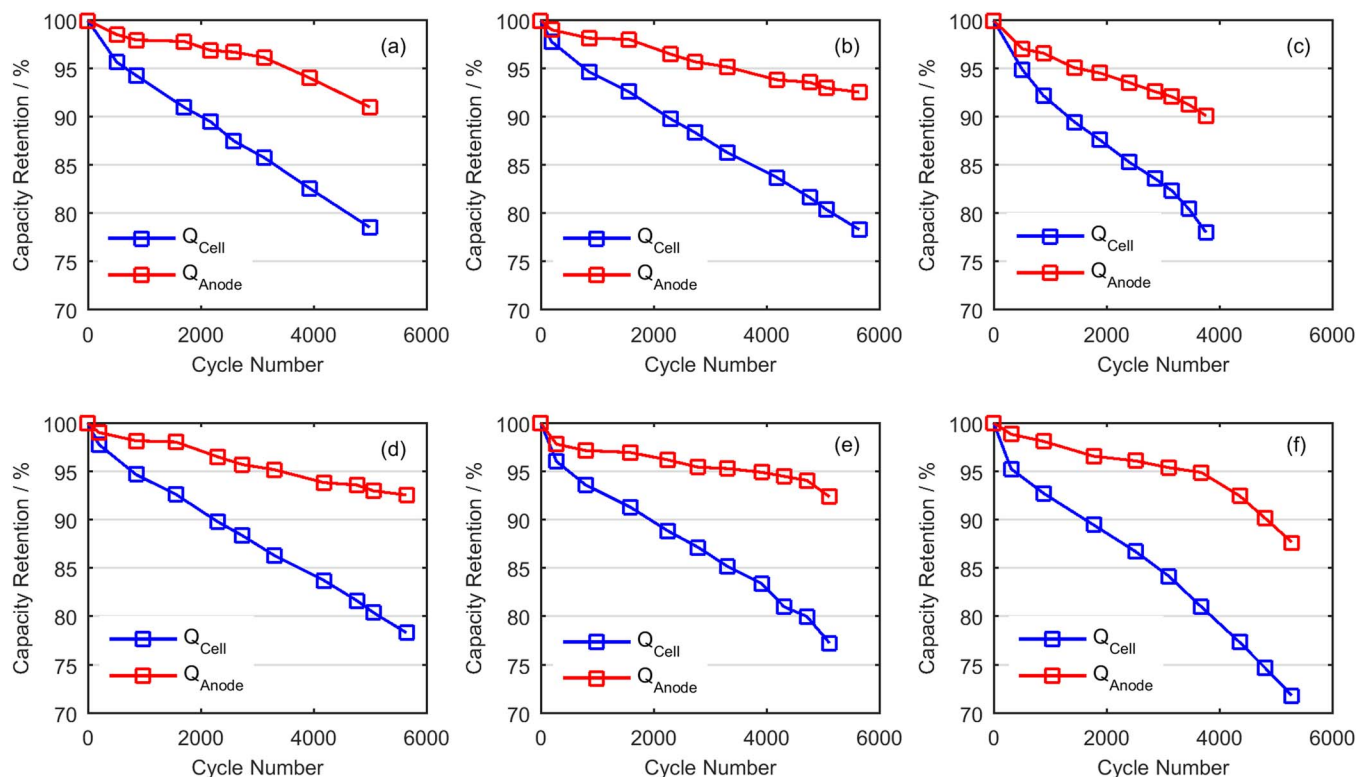


Figure 8. Capacity decrease and loss of anode active material of a cell cycled at (a) 10°C, 1C; (b) 25°C, 1C; (c) 40°C, 1C; (d) 25°C, 1C; (e) 25°C, 3C; (f) 25°C, 5C.

demonstrates satisfying stability under high C-rate discharge up to 5C. An accelerated capacity fade exists only in the first few hundred cycles and an almost identical capacity aging rate lasts for the rest cycle life. Unlike most studies, in which the discharge rate plays an exponential role in the capacity aging, the examined cell shows less discharge rate dependency probably thanks to its pouch cell design, which leads to less mechanical and thermal stress during cycling. Overall, a long cycle life of 3000–5000 cycles was achieved before reaching a capacity fade of 20%. The results of post-mortem studies will be presented in a subsequent article.

Acknowledgment

This work has been done in the framework of the research project ExZellTUM (03×4633A) funded by the German Federal Ministry of Education and Research (BMBF). The responsibility for this publication rests with the authors.

References

- J. Wang, P. Liu, J. Hicks-Garner, E. Sherman, S. Soukiazian, M. Verbrugge, H. Tatara, J. Musser, and P. Finamore, Cycle-life model for graphite-LiFePO₄ cells, *J. Power Sources*, **196**, 3942 (2011).
- M. Dubarry, C. Truchot, B. Y. Liaw, K. Gering, S. Sazhin, D. Jamison, and C. Michelbacher, Evaluation of commercial lithium-ion cells based on composite positive electrode for plug-in hybrid electric vehicle applications. Part II. Degradation mechanism under 2C cycle aging, *J. Power Sources*, **196**, 10336 (2011).
- M. Ecker, J. B. Gerschler, J. Vogel, S. Käbitz, F. Hust, P. Dechent, and D. U. Sauer, Development of a lifetime prediction model for lithium-ion batteries based on extended accelerated aging test data, *J. Power Sources*, **215**, 248 (2012).
- J. Schmalstieg, S. Käbitz, M. Ecker, and D. U. Sauer, A holistic aging model for Li(NiMnCo)O₂ based 18650 lithium-ion batteries, *J. Power Sources*, **257**, 325 (2014).
- S. F. Schuster, T. Bach, E. Fleder, J. Müller, M. Brand, G. Sextl, and A. Jossen, Non-linear aging characteristics of lithium-ion cells under different operational conditions, *J. Energy Storage*, **1**, 44 (2015).
- W. Prochazka, G. Pregartner, and M. Cifrain, Design-of-experiment and statistical modeling of a large scale aging experiment for two popular lithium ion cell chemistries, *J. Electrochem. Soc.*, **160**, A1039 (2013).
- T. Waldmann, M. Wilka, M. Kasper, M. Fleischhammer, and M. Wohlfahrt-Mehrens, Temperature dependent ageing mechanisms in Lithium-ion batteries - A Post-Mortem study, *J. Power Sources*, **262**, 129 (2014).
- M. Bauer, C. Guenther, M. Kasper, M. Petzl, and M. A. Danzer, Discrimination of degradation processes in lithium-ion cells based on the sensitivity of aging indicators toward capacity loss, *J. Power Sources*, **283**, 494 (2015).
- M. Petzl, M. Kasper, and M. A. Danzer, Lithium plating in a commercial lithium-ion battery - A low-temperature aging study, *J. Power Sources*, **275**, 799 (2015).
- C. Uhlmann, J. Illig, M. Ender, R. Schuster, and E. Ivers-Tiffée, In situ detection of lithium metal plating on graphite in experimental cells, *J. Power Sources*, **279**, 428 (2015).
- J. Wandt, C. Marino, H. A. Gasteiger, P. Jakes, R. -A. Eichel, and J. Granwehr, Operando electron paramagnetic resonance spectroscopy - formation of mossy lithium on lithium anodes during charge-discharge cycling, *Energ. Environ. Sci.*, **8**, 1358 (2015).
- D. Burrow, K. Sergeeva, S. Calles, K. Schorb, A. Börger, C. Roth, and P. Heitjans, Inhomogeneous degradation of graphite anodes in automotive lithium ion batteries under low-temperature pulse cycling conditions, *J. Power Sources*, **307**, 806 (2016).
- S. Schindler, M. Bauer, M. Petzl, and M. A. Danzer, Voltage relaxation and impedance spectroscopy as in-operando methods for the detection of lithium plating on graphitic anodes in commercial lithium-ion cells, *J. Power Sources*, **304**, 170 (2016).
- G. Ning, B. Haran, and B. N. Popov, Capacity fade study of lithium-ion batteries cycled at high discharge rates, *J. Power Sources*, **117**, 160 (2003).
- L. Lam and P. Bauer, Practical capacity fading model for Li-ion battery cells in electric vehicles, *IEEE Trans. Power Electron.*, **28**, 5910 (2013).
- N. Omar, M. A. Monem, Y. Firouz, J. Salminen, J. Smekens, O. Hegazy, H. Gaulous, G. Mulder, P. van den Bossche, T. Coosemans, and J. van Mierlo, Lithium iron phosphate based battery - Assessment of the aging parameters and development of cycle life model, *Appl. Energy*, **113**, 1575 (2014).
- Y. Cui, C. Du, G. Yin, Y. Gao, L. Zhang, T. Guan, L. Yang, and F. Wang, Multi-stress factor model for cycle lifetime prediction of lithium ion batteries with shallow-depth discharge, *J. Power Sources*, **279**, 123 (2015).
- A. Matasso, D. Wong, D. Wetz, and F. Liu, Effects of high-rate cycling on the bulk internal pressure rise and capacity degradation of commercial LiCoO₂ cells, *J. Electrochem. Soc.*, **162**, A885 (2015).
- D. Wong, B. Shrestha, D. A. Wetz, and J. M. Heinzel, Impact of high rate discharge on the aging of lithium nickel cobalt aluminum oxide batteries, *J. Power Sources*, **280**, 363 (2015).
- J. Wang, J. Purewal, P. Liu, J. Hicks-Garner, S. Soukiazian, E. Sherman, A. Sorenson, L. Vu, and H. Tatara, Degradation of lithium ion batteries employing graphite negatives and nickel-cobalt-manganese oxide + spinel manganese oxide positives - Part I Aging mechanisms and life estimation, *J. Power Sources*, **269**, 937 (2014).

21. B. Stiaszny, J. C. Ziegler, E. E. Krauß, M. Zhang, J. P. Schmidt, and E. Ivers-Tiffée, Electrochemical characterization and post-mortem analysis of aged LiMn_2O_4 -NMC/graphite lithium ion batteries - Part II Calendar aging, *J. Power Sources*, **258**, 61 (2014).
22. M. Ecker, N. Nieto, S. Käbitz, J. Schmalstieg, H. Blanke, A. Warnecke, and D. U. Sauer, Calendar and cycle life study of $\text{Li}(\text{NiMnCo})\text{O}_2$ -based 18650 lithium-ion batteries, *J. Power Sources*, **248**, 839 (2014).
23. H.-p. Lin, D. Chua, M. Salomon, H.-C. Shiao, M. Hendrickson, E. Plichta, and S. Slane, Low-temperature behavior of Li-ion cells, *Electrochem. Solid State Lett.*, **4**, A71 (2001).
24. C. T. Love, M. B. Virji, R. E. Rocheleau, and K. E. Swider-Lyons, State-of-health monitoring of 18650 4S packs with a single-point impedance diagnostic, *J. Power Sources*, **266**, 512 (2014).
25. K. Takeno, Quick testing of batteries in lithium-ion battery packs with impedance-measuring technology, *J. Power Sources*, **128**, 67 (2004).
26. D. Andre, M. Meiler, K. Steiner, C. Wimmer, T. Soczka-Guth, and D. U. Sauer, Characterization of high-power lithium-ion batteries by electrochemical impedance spectroscopy. I. Experimental investigation, *J. Power Sources*, **196**, 5334 (2011).
27. W. Waag, S. Käbitz, and D. U. Sauer, Experimental investigation of the lithium-ion battery impedance characteristic at various conditions and aging states and its influence on the application, *Appl. Energy*, **102**, 885 (2013).
28. J. Vetter, P. Novák, M. R. Wagner, C. Veit, K.-C. Möller, J. O. Besenhard, M. Winter, M. Wohlfahrt-Mehrens, C. Vogler, and A. Hammouche, Ageing mechanisms in lithium-ion batteries, *J. Power Sources*, **147**, 269 (2005).
29. E. Sarasketa-Zabala, I. Gandiaga, L. M. Rodriguez-Martinez, and I. Villarreal, Calendar ageing analysis of a LiFePO_4 /graphite cell with dynamic model validations - Towards realistic lifetime predictions, *J. Power Sources*, **272**, 45 (2014).
30. N. S. Hudak, L. E. Davis, and G. Nagasubramanian, Cycling-induced changes in the entropy profiles of lithium cobalt oxide electrodes, *J. Electrochem. Soc.*, **162**, A315 (2014).
31. D. Aurbach, B. Markovsky, M. Levi, E. Levi, A. Schechter, M. Moshkovich, and Y. Cohen, New insights into the interactions between electrode materials and electrolyte solutions for advanced nonaqueous batteries, *J. Power Sources*, 81–82, 95 (1999).
32. Q.-C. Zhuang, T. Wei, L.-L. Du, Y.-L. Cui, L. Fang, and S.-G. Sun, An electrochemical impedance spectroscopy study of the electronic and ionic transport properties of spinel LiMn_2O_4 , *J. Phys. Chem. C*, **114**, 8614 (2010).
33. H.-M. Cho, W.-S. Choi, J.-Y. Go, S.-E. Bae, and H.-C. Shin, A study on time-dependent low temperature power performance of a lithium-ion battery, *J. Power Sources*, **198**, 273 (2012).
34. A. Barai, G. H. Chouchelamane, Y. Guo, A. McGordon, and P. Jennings, A study on the impact of lithium-ion cell relaxation on electrochemical impedance spectroscopy, *J. Power Sources*, **280**, 74 (2015).
35. A. Jossen, Fundamentals of battery dynamics, *J. Power Sources*, **154**, 530 (2006).
36. S. Rodrigues, N. Munichandraiah, and A. K. Shukla, AC impedance and state-of-charge analysis of a sealed lithium-ion rechargeable battery, *J. Solid State Electrochem.*, **3**, 397 (1999).
37. L. Liao, P. Zuo, Y. Ma, X. Chen, Y. An, Y. Gao, and G. Yin, Effects of temperature on charge/discharge behaviors of LiFePO_4 cathode for Li-ion batteries, *Electrochim. Acta*, **60**, 269 (2012).
38. J. Gomez, R. Nelson, E. E. Kalu, M. H. Weatherspoon, and J. P. Zheng, Equivalent circuit model parameters of a high-power Li-ion battery - Thermal and state of charge effects, *J. Power Sources*, **196**, 4826 (2011).
39. Y.-M. Choi and S.-I. Pyun, Effects of intercalation-induced stress on lithium transport through porous LiCoO_2 electrode, *Solid State Ion.*, **99**, 173 (1997).
40. P. Arora, B. N. Popov, and R. E. White, Electrochemical investigations of cobalt-doped LiMn_2O_4 as cathode material for lithium-ion batteries, *J. Electrochem. Soc.*, **145**, 807 (1998).
41. M. Dubarry, C. Truchot, B. Y. Liaw, K. Gering, S. Sazhin, D. Jamison, and C. Michelbacher, Evaluation of commercial lithium-ion cells based on composite positive electrode for plug-in hybrid electric vehicle applications - III. Effect of thermal excursions without prolonged thermal aging, *J. Electrochem. Soc.*, **160**, A191 (2012).
42. X. Feng, J. Sun, M. Ouyang, X. He, L. Lu, X. Han, M. Fang, and H. Peng, Characterization of large format lithium ion battery exposed to extremely high temperature, *J. Power Sources*, **272**, 457 (2014).
43. J. Yamaki, Thermal stability of graphite anode with electrolyte in lithium-ion cells, *Solid State Ion.*, **148**, 241 (2002).
44. M. Zhou, L. Zhao, S. Okada, and J.-i. Yamaki, Quantitative studies on the influence of LFP on the thermal stability of graphite with electrolyte, *J. Electrochem. Soc.*, **159**, A44 (2012).
45. H. J. Ploehn, P. Ramadass, and R. E. White, Solvent diffusion model for aging of lithium-ion battery cells, *J. Electrochem. Soc.*, **151**, A456 (2004).
46. M. B. Pinson and M. Z. Bazant, Theory of SEI formation in rechargeable batteries - capacity fade, accelerated aging and lifetime prediction, *J. Electrochem. Soc.*, **160**, A243 (2013).
47. M.-S. Wu, P.-C. J. Chiang, and J.-C. Lin, Electrochemical investigations on capacity fading of advanced lithium-ion batteries by three-electrode measurements, *J. Electrochem. Soc.*, **152**, A47 (2005).
48. T. Nonaka, C. Okuda, Y. Seno, Y. Kondo, K. Koumoto, and Y. Ukyo, Surface sensitive X-ray absorption study on NCA cathode material for lithium ion batteries, *J. Electrochem. Soc.*, **154**, A353 (2007).
49. J. Zhou and P. Notten, Studies on the degradation of Li-ion batteries by the use of microreference electrodes, *J. Power Sources*, **177**, 553 (2008).
50. S. Watanabe, M. Kinoshita, T. Hosokawa, K. Morigaki, and K. Nakura, Capacity fade of $\text{LiAl}_y\text{Ni}_{1-x-y}\text{Co}_x\text{O}_2$ cathode for lithium-ion batteries during accelerated calendar and cycle life tests (surface analysis of $\text{LiAl}_y\text{Ni}_{1-x-y}\text{Co}_x\text{O}_2$ cathode after cycle tests in restricted depth of discharge ranges), *J. Power Sources*, **258**, 210 (2014).
51. K. Kleiner, D. Dixon, P. Jakes, J. Melke, M. Yavuz, C. Roth, K. Nikolowski, V. Liebau, and H. Ehrenberg, Fatigue of $\text{LiNi}_{0.8}\text{Co}_{0.15}\text{Al}_{0.05}\text{O}_2$ in commercial Li ion batteries, *J. Power Sources*, **273**, 70 (2015).
52. D. Mohanty, K. Dahlberg, D. M. King, L. A. David, A. S. Sefat, D. L. Wood, C. Daniel, S. Dhar, V. Mahajan, M. Lee, and F. Albano, Modification of Ni-rich FCG NMC and NCA cathodes by atomic layer deposition: Preventing surface phase transitions for high-voltage lithium-ion batteries, *Sci. Rep.*, **6**, 26532 (2016).
53. C. R. A. Clauss and H. E. L. G. Schweigart, The reduction of manganese dioxide in Leclanché-type dry cells as displayed by derivative discharge functions, *J. Electrochem. Soc.*, **123**, 951 (1976).
54. M. Dubarry, V. Svoboda, R. Hwu, and B. Yann Liaw, Incremental capacity analysis and close-to-equilibrium OCV measurements to quantify capacity fade in commercial rechargeable lithium batteries, *Electrochem. Solid-State Lett.*, **9**, A454 (2006).
55. M. Dubarry, V. Svoboda, R. Hwu, and B. Y. Liaw, Capacity and power fading mechanism identification from a commercial cell evaluation, *J. Power Sources*, **165**, 566 (2007).
56. M. Dubarry, V. Svoboda, R. Hwu, and B. Y. Liaw, Capacity loss in rechargeable lithium cells during cycle life testing - The importance of determining state-of-charge, *J. Power Sources*, **174**, 1121 (2007).
57. M. Dubarry and B. Y. Liaw, Identify capacity fading mechanism in a commercial LiFePO_4 cell, *J. Power Sources*, **194**, 541 (2009).
58. M. Dubarry, B. Y. Liaw, M.-S. Chen, S.-S. Chyan, K.-C. Han, W.-T. Sie, and S.-H. Wu, Identifying battery aging mechanisms in large format Li ion cells, *J. Power Sources*, **196**, 3420 (2011).
59. M. Dubarry, C. Truchot, M. Cugnet, B. Y. Liaw, K. Gering, S. Sazhin, D. Jamison, and C. Michelbacher, Evaluation of commercial lithium-ion cells based on composite positive electrode for plug-in hybrid electric vehicle applications. Part I - Initial characterizations, *J. Power Sources*, **196**, 10328 (2011).
60. M. Dubarry, C. Truchot, and B. Y. Liaw, Synthesize battery degradation modes via a diagnostic and prognostic model, *J. Power Sources*, **219**, 204 (2012).
61. M. Dubarry, C. Truchot, and B. Y. Liaw, Cell degradation in commercial LiFePO_4 cells with high-power and high-energy designs, *J. Power Sources*, **258**, 408 (2014).
62. I. Bloom, J. Christophersen, and K. Gering, Differential voltage analyses of high-power lithium-ion cells, *J. Power Sources*, **139**, 304 (2005).
63. I. Bloom, J. P. Christophersen, D. P. Abraham, and K. L. Gering, Differential voltage analyses of high-power lithium-ion cells, *J. Power Sources*, **157**, 537 (2006).
64. I. Bloom, A. N. Jansen, D. P. Abraham, J. Knuth, S. A. Jones, V. S. Battaglia, and G. L. Henriksen, Differential voltage analyses of high-power, lithium-ion cells, *J. Power Sources*, **139**, 295 (2005).
65. I. Bloom, L. K. Walker, J. K. Basco, D. P. Abraham, J. P. Christophersen, and C. D. Ho, Differential voltage analyses of high-power lithium-ion cells. 4. Cells containing NMC, *J. Power Sources*, **195**, 877 (2010).
66. H. M. Dahn, A. J. Smith, J. C. Burns, D. A. Stevens, and J. R. Dahn, User-friendly differential voltage analysis freeware for the analysis of degradation mechanisms in Li-ion batteries, *J. Electrochem. Soc.*, **159**, A1405 (2012).
67. M. Kassem, J. Bernard, R. Revel, S. Pélissier, F. Duclaud, and C. Delacourt, Calendar aging of a graphite/ LiFePO_4 cell, *J. Power Sources*, **208**, 296 (2012).
68. X. Han, M. Ouyang, L. Lu, J. Li, Y. Zheng, and Z. Li, A comparative study of commercial lithium-ion battery cycle life in electrical vehicle - Aging mechanism identification, *J. Power Sources*, **251**, 38 (2014).
69. Z. Ma, J. Jiang, W. Shi, W. Zhang, and C. C. Mi, Investigation of path dependence in commercial lithium-ion cells for pure electric bus applications - Aging mechanism identification, *J. Power Sources*, **274**, 29 (2015).
70. J. P. Schmidt, H. Y. Tran, J. Richter, E. Ivers-Tiffée, and M. Wohlfahrt-Mehrens, Analysis and prediction of the open circuit potential of lithium-ion cells, *J. Power Sources*, **239**, 696 (2013).
71. T. Kobayashi, N. Kawasaki, Y. Kobayashi, K. Shono, Y. Mita, and H. Miyashiro, A method of separating the capacities of layer and spinel compounds in blended cathode, *J. Power Sources*, **245**, 1 (2014).
72. P. Keil, S. F. Schuster, W. Jörn, J. Travi, A. Hauser, R. C. Karl, and A. Jossen, Calendar aging of lithium-ion batteries - Impact of the graphite anode on capacity fade, *J. Electrochem. Soc.*, **163**, A1872 (2016).
73. P. Keil and A. Jossen, Calendar aging of NCA lithium-ion batteries investigated by differential voltage analysis and coulomb tracking, *J. Electrochem. Soc.*, **164**, A6066 (2016).
74. M. Dubarry, P. Cabanel, and B. Y. Liaw, Intrinsic degradation variability in commercial lithium-ion batteries, Abstract #A01-0129, 228th ECS Meeting, Phoenix, AZ, Oct 11-16, 2015.